The Astrophysical Journal Supplement Series, 222:2 (13pp), 2016 January doi:10.3847/0067-0049/222/1/2

NEAR-INFRARED POLARIZATION SOURCE CATALOG OF THE NORTHEASTERN REGIONS OF THE LARGE MAGELLANIC CLOUD

Jaeyeong Kim[1], Woong-Seob Jeong[2,3], Soojong Pak[1], Won-Kee Park[2], and Motohide Tamura[4]
[1] School of Space Research, Kyung Hee University, 1 Seocheon-dong, Giheung-gu, Yongin, Gyeonggi-do 446-701, Korea; jaeyeong@khu.ac.kr
[2] Korea Astronomy and Space Science Institute, 776 Daedeok-daero, Yuseong-gu, Daejeon 305-348, Korea; jeongws@kasi.re.kr
[3] Korea University of Science and Technology, 217 Gajeong-ro, Yuseong-gu, Daejeon 305-350, Korea
[4] The University of Tokyo/National Astronomical Observatory of Japan/Astrobiology Center, 2-21-1 Osawa, Mitaka, Tokyo 181-8588, Japan
Received 2015 July 1; accepted 2015 November 15; published 2016 January 8

ABSTRACT

We present a near-infrared band-merged photometric and polarimetric catalog for the $39' \times 69'$ fields in the northeastern part of the Large Magellanic Cloud (LMC), which were observed using SIRPOL, an imaging polarimeter of the InfraRed Survey Facility. This catalog lists 1858 sources brighter than 14 mag in the H band with a polarization signal-to-noise ratio greater than three in the J, H, or K_s bands. Based on the relationship between the extinction and the polarization degree, we argue that the polarization mostly arises from dichroic extinctions caused by local interstellar dust in the LMC. This catalog allows us to map polarization structures to examine the global geometry of the local magnetic field, and to show a statistical analysis of the polarization of each field to understand its polarization properties. In the selected fields with coherent polarization position angles, we estimate magnetic field strengths in the range of $3-25\ \mu$G using the Chandrasekhar–Fermi method. This implies the presence of large-scale magnetic fields on a scale of around 100 parsecs. When comparing mid- and far-infrared dust emission maps, we confirmed that the polarization patterns are well aligned with molecular clouds around the star-forming regions.

Key words: infrared: ISM – infrared: stars – ISM: magnetic fields – ISM: structure – Magellanic Clouds – polarization

Supporting material: machine-readable table

1. INTRODUCTION

Magnetic fields are important for understanding galactic dynamics and star formation processes. To date, various methods for measuring interstellar magnetic fields have been devised to probe the star-forming regions in our Galaxy and in external galaxies (Davis & Greenstein 1951; Vrba et al. 1976; Lazarian 2007). When background starlight passes through dust grains aligned with the local magnetic field, the light is linearly polarized by dichroic extinction parallel to the grain's long axis.

The Large Magellanic Cloud (LMC) is a unique target for studying magnetic fields and star-forming processes. Due to its proximity and face-on orientation, we can trace its large-scale interactions with the halo of the Milky Way and the Small Magellanic Cloud, and small-scale structures of the local star-forming regions (Kim et al. 1998, 2011; Pak et al. 1998). Previous studies of magnetic fields in the LMC were carried out using multi-frequency surveys of diffuse synchrotron emission in radio bands (Wayte 1990; Haynes et al. 1991; Gaensler et al. 2005; Mao et al. 2012). Optical polarization (Visvanathan 1966; Mathewson & Ford 1970; Schmidt 1970, 1976) has demonstrated the existence of large-scale magnetic fields in the LMC. However, these results were restricted only to bright stars. Wisniewski et al. (2007, hereafter W07) also showed the detailed polarization map of NGC 2100 on the eastern side of 30 Doradus and its surrounding regions in optical bands. The near-infrared band has an advantage over the optical band because the background starlight in star-forming regions suffers heavy extinction (Tamura et al. 1987, 1988; Sato et al. 1988). Nakajima et al. (2007, hereafter N07) studied magnetic field structures $7\farcm7 \times 7\farcm7$ around 30 Doradus using near-IR polarimetry. They revealed more detailed magnetic field structures that are aligned roughly in the east–west direction compared to the previous results in the optical band (Visvanathan 1966; Mathewson & Ford 1970; Schmidt 1970). These field structures are associated with expanding shells around 30 Doradus.

We carried out a near-IR photometric and polarimetric study of the $39' \times 69'$ fields in the northeastern part of the LMC. The target fields contain four important star-forming regions, 30 Doradus, N158, N159, and N160. The initial investigation of the polarimetric data around 30 Doradus was presented in Kim et al. (2011). However, the survey was limited to a $20' \times 20'$ region and the data were hampered by unstable weather conditions. In this paper, we analyze additional data sets for more regions. The procedures to obtain the photometric results are described in Section 2. We compile photometric and polarimetric data for each observation field in a catalog. In Section 3, we examine the origin of the polarization based on wavelength dependence. In Section 4, we show polarization vector maps for each observation field and discuss the related magnetic field structures. We also calculate magnetic field strengths in five sample fields. Finally, we discuss the correlation of our polarization results with dust emission and CO distribution.

2. OBSERVATIONS AND DATA REDUCTION

2.1. Observational Information

We observed the northeastern regions of the LMC using the infrared camera SIRIUS (Nagayama et al. 2003) and the polarimeter SIRPOL (Kandori et al. 2006) at the Infrared Survey Facility (IRSF) 1.4 m telescope at the South African Astronomical Observatory (SAAO) on 2008 December 25–30

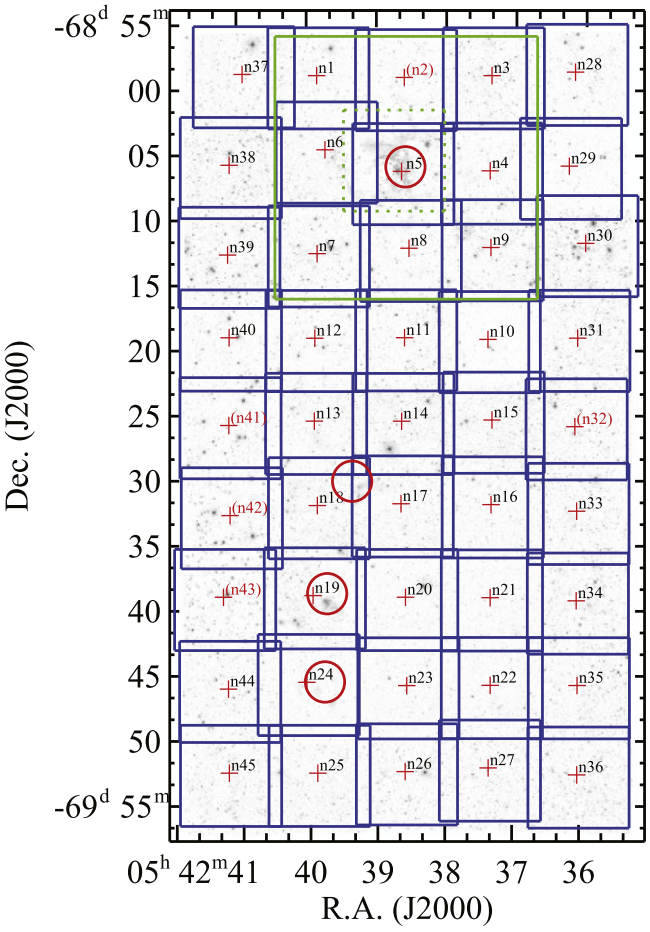

Figure 1. Observed fields in the northeastern regions of the LMC. The figure shows a total of 5 × 9 fields observed with SIRPOL on 2008 December 25, 26, 27, and 30, and 2011 December 10 and 11. Red open circles represent star-forming regions: 30 Doradus, N158, N160, and N159, moving from north to south. The field center and area (7.′7 × 7.′7) are displayed as a red cross and a blue box, respectively. The fields of view covered by N07 and Kim et al. (2011) are also highlighted as green dotted and solid boxes, respectively. Field numbers in parentheses denote the discarded fields due to unstable weather conditions.

and 2011 December 2−11. This system has a field of view of (7.′7 × 7.′7) and a pixel scale of 0.″45 pixel^{-1}. One data set for a target field consists of 20 s exposures at 10 dithered positions for four wave-plate angles (0°, 45°, 22.°5, and 67.°5) in the J (1.25 μm), H (1.63 μm), and K_s (2.14 μm) bands. The target regions of 39′ × 69′ are tiled with 45 fields with grid spacings of 6.′5 × 6.′5 (Figure 1). We provide the observation log in Table 1.

2.2. Data Reduction Procedure

We used the SIRPOL data reduction pipeline (Kandori et al. 2006) at the Image Reduction & Analysis Facility[5] (IRAF). The pipeline incorporates the following procedures: flat field correction, sky subtraction, and combining of dithered frames. We checked the output magnitude variations in 40 sequential frames to filter bad data affected by non-photometric weather. Those fields with magnitude variations larger than 0.03 mag were rejected (see Figure 1).

We used Source Extractor (SExtractor) for source detection and aperture photometry (Bertin & Arnouts 1996). Various SExtractor parameters were optimized (i.e., a detection threshold of 5σ, a background box size of 16 pixels, a background filter of 3 × 3 meshes, and an aperture diameter of 8 pixels). We measured the instrumental magnitudes of stars for four wave-plate angles in the J, H, and K_s bands. The pixel coordinates of the sources were converted to celestial coordinates using the 2MASS All Sky Point Source Catalog (Skrutskie et al. 2006). The instrumental magnitude and color were calibrated using the equations below:

$$M_{\rm 2MASS} = M_{\rm IRSF} + \alpha_1 \times C_{\rm IRSF} + \beta_1, \quad (1)$$

$$C_{\rm 2MASS} = \alpha_2 \times C_{\rm IRSF} + \beta_2, \quad (2)$$

where $M_{\rm IRSF}$ and $C_{\rm IRSF}$ are the instrumental magnitudes and colors from the Stokes I images, and $M_{\rm 2MASS}$ and $C_{\rm 2MASS}$ are the magnitude and color in the 2MASS system. The transformation coefficients, α and β, for each field were estimated using a robust least absolute deviation method.

We calculated the polarization of point sources using the Stokes parameters I, Q, and U as described by Kim et al. (2011). The flux errors of sources at each wave-plate angle (0°, 45°, 22.°5, and 67.°5) are described as σ_{I_1}, σ_{I_2}, σ_{I_3}, and σ_{I_4}, respectively. The uncertainty for P (%) was derived as follows:

$$\overline{\sigma}_Q = \sqrt{\left(\frac{\sigma_Q}{I}\right)^2 + \left(\frac{Q}{I^2} \times \sigma_I\right)^2}, \quad (3)$$

$$\overline{\sigma}_U = \sqrt{\left(\frac{\sigma_U}{I}\right)^2 + \left(\frac{U}{I^2} \times \sigma_I\right)^2}, \quad (4)$$

$$\sigma_P = \frac{\sqrt{\left(\frac{Q}{I}\right)^2 \times \overline{\sigma}_Q^2 + \left(\frac{U}{I}\right)^2 \times \overline{\sigma}_U^2}}{P}, \quad (5)$$

where $\overline{\sigma}_Q$ and $\overline{\sigma}_U$ are normalized errors with I. The errors of Stokes parameters σ_I, σ_Q, and σ_U can be written as $\sqrt{\sigma_Q^2 + \sigma_U^2}/2$, $\sqrt{\sigma_{I_1}^2 + \sigma_{I_2}^2}$, and $\sqrt{\sigma_{I_3}^2 + \sigma_{I_4}^2}$, respectively.

3. RESULTS

3.1. Estimation of the Photometric and the Polarimetric Accuracy

A total of 25,488 sources were detected with SExtractor. To verify the photometric accuracy, we compared our data set with the IRSF Magellanic Cloud point-source catalog (hereafter the IRSF catalog) in Kato et al. (2007). The IRSF catalog provides photometry results in the J, H, and K_s bands. Figure 2 shows a histogram of the position offsets of our sources that matched theirs. Most sources have an offset around 0.″1 and we retain only those sources with an offset of less than 0.″3. The proper motion effect between two data sets is negligible: $\mu_\alpha \cos\delta = 1.89 \pm 0.27$ mas yr^{-1} and $\mu_\delta = 0.39 \pm 0.27$ mas yr^{-1} (Vieira et al. 2010). The magnitude differences between the IRSF catalog and ours are shown in Figure 3. Most sources brighter than 14 mag have differences in magnitude from the IRSF catalog of less than 0.3 mag in the J, H, and K_s bands.

The polarization uncertainty with magnitude is shown in Figure 4. Among the sources with P/σ_P (polarization signal-to-noise ratio) greater than 10, the polarization uncertainty is

[5] IRAF is distributed by the US National Optical Astronomy Observatories, which are operated by the Association of Universities for Research in Astronomy, Inc., under cooperative agreement with the National Science Foundation.

Table 1
Observation Log

Field Name	$\alpha_{\rm oJ2000.0}$	$\delta_{\rm oJ2000.0}$	Date (LT)	Seeing in J ($''$)	Magnitude variation (mag)
n1	05 39 54.4	−68 59 20.0	2008 Dec 30	1.70	0.022
n3	05 37 25.6	−68 59 19.9	2008 Dec 30	1.65	0.022
n4	05 37 25.2	−69 06 00.5	2008 Dec 25	1.58	0.023
n5	05 38 40.1	−69 06 00.0	2008 Dec 25	1.67	0.029
n6	05 39 54.8	−69 06 00.1	2008 Dec 25	1.68	0.024
n7	05 39 55.1	−69 12 40.2	2008 Dec 25	1.51	0.016
n8	05 38 40.1	−69 12 40.1	2008 Dec 25	1.54	0.022
n9	05 37 25.0	−69 12 39.9	2008 Dec 25	1.45	0.026
n10	05 37 24.6	−69 19 19.9	2008 Dec 25	1.91	0.023
n11	05 38 40.0	−69 19 20.2	2008 Dec 25	2.46	0.024
n12	05 39 55.6	−69 19 20.1	2008 Dec 25	1.62	0.023
…	…	…	2011 Dec 11	1.48	0.024
n13	05 39 56.0	−69 26 00.4	2008 Dec 26	2.07	0.019
…	…	…	2011 Dec 11	1.24	0.024
n14	05 38 40.1	−69 26 00.0	2008 Dec 26	1.71	0.021
…	…	…	2011 Dec 11	1.39	0.021
n15	05 37 24.2	−69 25 59.9	2008 Dec 26	1.80	0.023
…	…	…	2011 Dec 11	1.22	0.021
n16	05 37 23.7	−69 32 39.9	2008 Dec 26	2.10	0.023
…	…	…	2011 Dec 11	1.04	0.021
n17	05 38 40.2	−69 32 40.0	2011 Dec 11	1.11	0.025
n18	05 39 56.4	−69 32 40.1	2011 Dec 11	1.07	0.025
n19	05 39 56.8	−69 39 20.2	2011 Dec 11	1.31	0.026
n20	05 38 40.1	−69 39 20.0	2011 Dec 11	1.20	0.023
n21	05 37 23.3	−69 39 20.0	2011 Dec 11	1.26	0.022
n22	05 37 23.0	−69 46 00.4	2008 Dec 27	1.41	0.023
…	…	…	2011 Dec 11	1.26	0.024
n23	05 38 40.1	−69 46 00.2	2008 Dec 27	1.94	0.018
…	…	…	2011 Dec 11	1.15	0.026
n24	05 39 57.1	−69 46 00.1	2011 Dec 11	1.34	0.028
n25	05 39 57.5	−69 52 40.0	2011 Dec 11	1.22	0.029
n26	05 38 40.1	−69 52 40.3	2011 Dec 10	2.18	0.024
n27	05 37 22.6	−69 52 40.8	2008 Dec 30	1.78	0.021
…	…	…	2011 Dec 10	2.05	0.025
n28	05 36 11.3	−68 59 19.9	2011 Dec 10	1.71	0.026
n29	05 36 10.7	−69 06 00.3	2011 Dec 10	1.48	0.026
n30	05 36 09.8	−69 12 39.9	2008 Dec 25	1.74	0.027
n31	05 36 09.1	−69 19 20.1	2008 Dec 25	1.87	0.026
n33	05 36 07.4	−69 32 40.0	2008 Dec 26	1.60	0.023
n34	05 36 06.7	−69 39 20.1	2008 Dec 27	1.63	0.022
n35	05 36 05.8	−69 46 00.3	2008 Dec 27	1.62	0.023
n36	05 36 05.5	−69 52 40.1	2011 Dec 10	1.81	0.024
n37	05 41 08.8	−68 59 19.9	2008 Dec 30	1.64	0.024
n38	05 41 09.5	−69 05 59.8	2008 Dec 25	1.53	0.019
n39	05 41 10.4	−69 12 40.1	2008 Dec 25	1.58	0.020
n40	05 41 11.0	−69 19 20.1	2008 Dec 25	2.17	0.019
n44	05 41 14.2	−69 46 00.2	2008 Dec 30	1.77	0.019
n45	05 41 15.0	−69 52 40.3	2008 Dec 30	1.73	0.025

Note. Data from 2 to 9 on 2011 December were discarded due to an instrumental problem during the observation.

lower than 1% for sources brighter than 14.5 mag (Figure 4(a)). We also compared polarimetric results with previous studies. N07 had observed the central $7\farcm7 \times 7\farcm7$ (one field) region of 30 Doradus using the same SIRIUS/SIRPOL system. The integration time of 1480 s per wave-plate angle makes N07 a very good reference for verifying the polarimetric accuracy of our data. We examined the polarimetric results for $P/\sigma_P > 3$ between N07 and our 30 Doradus field, and Figure 5 shows the comparison results. The difference in polarization degree increases at around 14 mag in the J and H bands. Although the difference in the polarization angle shows some notable scatter over the entire range of magnitude, the scatter is quite constant down to 14 mag in the J and H bands.

As a result, we adopted all of the sources brighter than 14 mag in the H band. In order to increase the number of meaningful sources, we extended the criteria of P/σ_P to include $3'$. Most sources in Figure 4(b) have their polarization uncertainties $\leqslant$2% for sources brighter than 14 mag. Typical polarization uncertainties between 13.9 and 14.1 mag in the H band are 1.12 ± 0.25, 0.74 ± 0.06, and 1.68 ± 0.27% in the J, H, and K_s bands, respectively. We checked the accuracy of the polarization position angles for the selected data by comparing

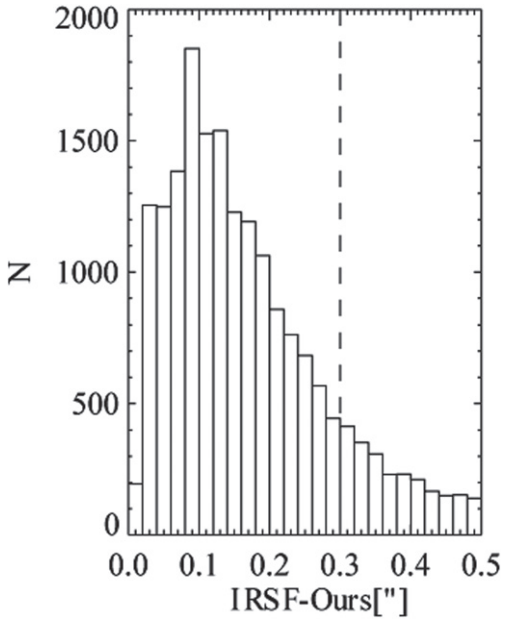

Figure 2. Histogram of position offsets between the IRSF catalog and our sources. Distribution peak is around 0.″1. The vertical dashed line indicates our matching criterion for the catalog.

differences in the polarization position angles among the three bands. The upper and lower panels of Figure 6 show the distribution of polarization position angles for the J versus H band and the H versus K_s band, respectively. The estimated uncertainty of the polarization position angles is smaller than 10°. As seen in Figure 6, we confirm that most of the sources in our catalog show consistent polarization position angles (within one standard deviation) from the correlation slope.

3.2. Catalog

The final catalog includes all of the reliable sources. Among the 25,488 detected sources, 1858 sources were selected based on the following criteria: $m_H < 14$ mag and $P/\sigma_P > 3$ for at least one band, where σ_P indicates the polarization uncertainty. Table 2 lists the photometric and polarimetric results for the compiled catalog sources. In addition, we compiled the proper motion data from Southern Proper Motion (SPM) material (Vieira et al. 2010). Information for each column of the table is given below:

Column (1) Observation field names that include observation date;
Column (2) Source ID; the formats referred to the equatorial coordinates;
Columns (3)–(4) Equatorial coordinates (J2000.0) in decimal degrees;
Columns (5)–(10) J, H, and K_s magnitude and error;
Columns (11)–(16) J, H, and K_s polarization degree and error in units of percentage;
Columns (17)–(22) J, H, and K_s polarization position angle and error in units of degrees;
Columns (23)–(24) Absolute proper motion in right ascension and error in units of mas yr^{-1} from SPM catalog;
Columns (25)–(26) Absolute proper motion in declination and error in units of mas yr^{-1} from SPM catalog;
Columns (27)–(28) Johnson B and V magnitude from SPM catalog.

3.3. Polarization Relationship between the J, H, and K_s Bands

Serkowski et al. (1975) first formulated the wavelength dependence of interstellar polarization in the Galaxy, and Whittet & van Breda (1978) modified the empirical relationship between the wavelength and the size of the dust grains. The modified "Serkowski law" was represented by a power-law dependence of the polarization as below:

$$P_\lambda \propto \lambda^{-\beta} \tag{6}$$

with β of 1.6−2.0 in the near-IR ($1.25 \leqslant \lambda \leqslant 2.2$) in previous studies (Martin & Whittet 1990; Nagata 1990; Martin et al. 1992). For the 30 Doradus region, N07 presented a slightly different power-law index of $\beta = 0.9$. As seen in Figure 7, our result is consistent with that of N07. For your reference, we also plot those sources matched with the *AKARI* LMC point-source catalog to check for the possibility of intrinsic polarization (see Section 3.4 for details).

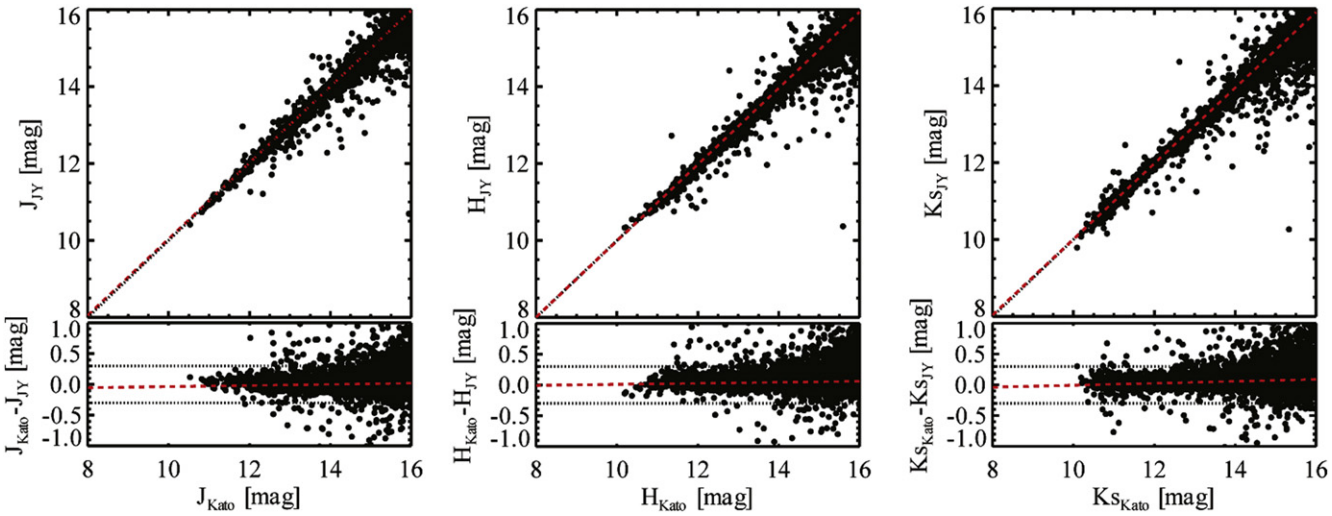

Figure 3. Magnitude differences of sources between the IRSF catalog and ours as a function of magnitude in the J (left), H (middle), and K_S (right) bands. Black dotted lines in the lower panels indicate the magnitude difference of 0.3 mag. All red dashed lines indicate results of least-square fitting for the sources.

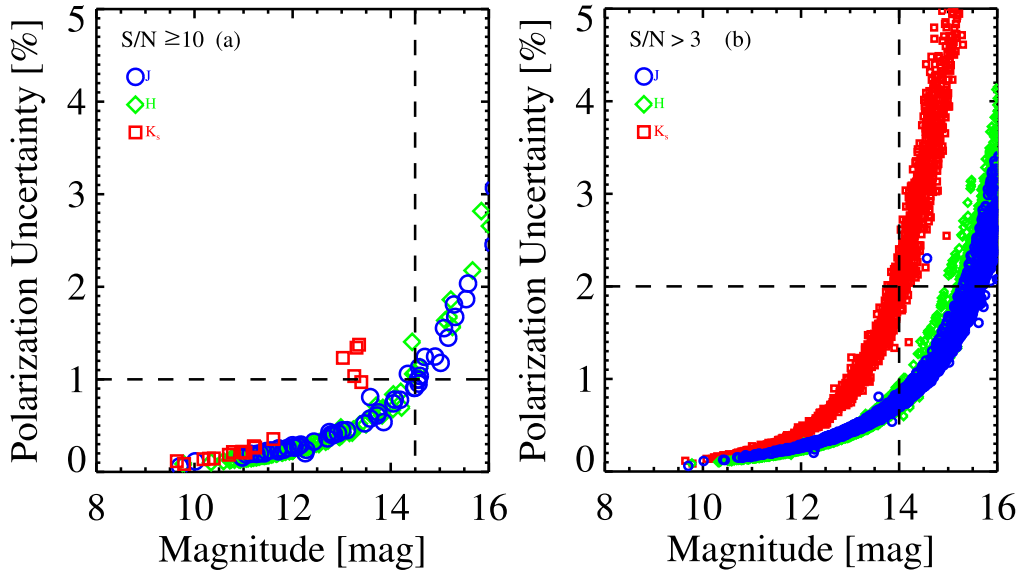

Figure 4. Polarization uncertainty as a function of magnitude in the J (*circle*), H (*diamond*), and K_S (*box*) bands. (a) The sources with polarization signal-to-noise ratio $P/\sigma_P \geqslant 10$ are included in the figure. Under 14.5 mag (vertical dashed line), most sources have an uncertainty of polarization degree smaller than 1% (horizontal dashed line). (b) The sources with a polarization signal-to-noise ratio $P/\sigma_P > 3$ are included in the figure. Under 14 mag (vertical dashed line), most sources have an uncertainty of polarization degree smaller than 2% (horizontal dashed line).

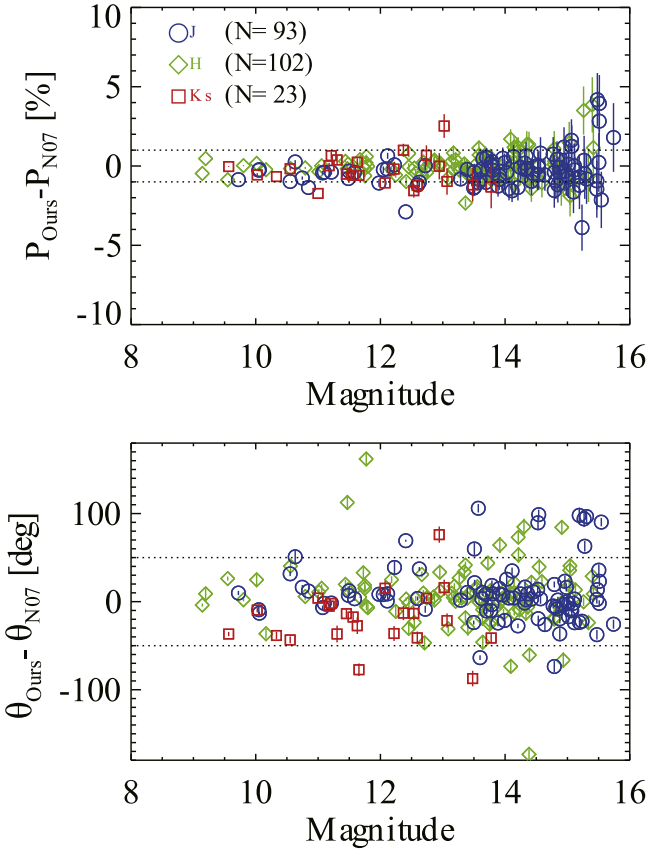

Figure 5. Polarization degree (top) and position angle (bottom) differences of sources matched between N07 and ours in 30 Doradus as a function of magnitudes in the J (*circle*), H (*diamond*), and K_S (*box*) bands. Scattered ranges of the sources brighter than 14 mag at the polarization degree and position angle are denoted by dotted lines.

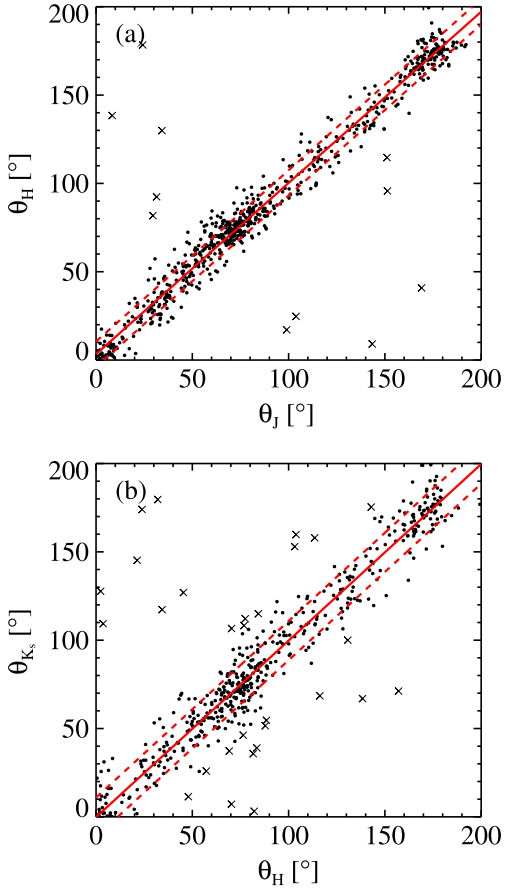

Figure 6. Polarization position angle difference with (a) J vs. H band and (b) H vs. K_s band for 697 and 508 sources, respectively. These sources are selected from the following criteria: $m_H < 14$ mag and $P/\sigma_P > 3$. Both figures show similar distributions for the polarization position angles within one standard deviation (red dashed lines) from the correlation slope (red solid line) of (a) and (b), respectively. The cross symbol shows a rejected source where the deviation of the polarization position angle from the fitted line is greater than 30°. Most of the sources in our catalog have an uncertainty in polarization position angles smaller than 10°.

Table 2
Photometric and Polarimetric Catalog of the Sources in the Northeastern Regions of the LMC[a]

Field ID	Source ID	Position		Magnitude						Polarization Properties												SPM Data					
		$\alpha_{\circ J2000.0}$	$\delta_{\circ J2000.0}$	J (mag)		H (mag)		K_s (mag)		P_J (%)		P_H (%)		P_{K_S} (%)		θ_J (°)		θ_H (°)		θ_{K_S} (°)		$\mu_\alpha \cos\delta$ (mas yr^{-1})		μ_δ (mas yr^{-1})		B (mag)	V (mag)
(1)	(2)	(3)	(4)	(5)	(6)	(7)	(8)	(9)	(10)	(11)	(12)	(13)	(14)	(15)	(16)	(17)	(18)	(19)	(20)	(21)	(22)	(23)	(24)	(25)	(26)	(27)	(28)
LMC_n1_081230	05394434-6902386	05 39 44.34	−69 02 38.53	14.588	0.010	13.877	0.004	13.641	0.017	<	2.92	<	1.98	5.02	1.45	⋯	⋯	⋯	⋯	120.01	7.93	13.19	26.86	−8.20	25.76	18.31	18.37
LMC_n1_081230	05402245-6855536	05 40 22.44	−68 55 53.55	12.122	0.003	11.108	0.001	10.799	0.003	<	0.81	0.67	0.15	<	0.57	⋯	⋯	134.86	6.37	⋯	⋯	5.92	10.72	−0.96	10.56	18.51	16.51
LMC_n1_081230	05395766-6855594	05 39 57.65	−68 55 59.29	13.193	0.005	11.725	0.002	11.120	0.003	<	1.35	0.73	0.22	<	0.60	⋯	⋯	144.33	8.20	⋯	⋯	−9.49	26.88	−1.86	25.79	24.42	18.37
LMC_n1_081230	05402167-6856250	05 40 21.66	−68 56 24.92	14.665	0.011	13.805	0.004	13.562	0.016	<	3.03	2.08	0.63	<	4.03	⋯	⋯	143.81	8.28	⋯	⋯	⋯	⋯	⋯	⋯	⋯	⋯
LMC_n1_081230	05402523-6856327	05 40 25.21	−68 56 32.80	14.384	0.009	13.413	0.003	13.133	0.012	<	2.58	2.59	0.50	<	2.77	⋯	⋯	136.25	5.44	⋯	⋯	⋯	⋯	⋯	⋯	⋯	⋯
LMC_n1_081230	05401186-6856470	05 40 11.86	−68 56 46.89	14.456	0.009	13.557	0.003	13.324	0.013	<	2.68	2.06	0.54	<	3.26	⋯	⋯	122.63	7.27	⋯	⋯	−2.41	18.63	34.94	17.99	18.95	17.93
LMC_n1_081230	05402353-6856500	05 40 23.54	−68 56 49.85	13.096	0.005	12.467	0.002	12.248	0.007	<	1.32	1.16	0.30	<	1.47	⋯	⋯	135.02	7.08	⋯	⋯	2.90	8.05	9.60	8.07	16.37	15.02
LMC_n1_081230	05401208-6857259	05 40 12.07	−68 57 25.83	12.555	0.004	11.610	0.001	11.348	0.004	<	1.00	0.79	0.19	<	0.81	⋯	⋯	124.71	6.81	⋯	⋯	0.52	9.38	2.91	9.33	18.08	15.64
LMC_n1_081230	05392139-6857262	05 39 21.40	−68 57 25.97	14.045	0.008	13.412	0.003	13.192	0.012	<	2.15	<	1.49	3.39	0.99	⋯	⋯	⋯	⋯	137.16	8.03	2.79	11.54	19.50	11.31	17.50	16.87
LMC_n1_081230	05394537-6857279	05 39 45.37	−68 57 27.95	11.782	0.003	11.298	0.001	11.121	0.003	0.78	0.23	0.98	0.16	1.16	0.24	148.45	8.16	143.67	4.72	137.73	5.85	2.44	5.90	−11.26	5.99	13.99	13.10

Notes. For sources with $P/\sigma_P \leqslant 3$, the $3\sigma_P$ upper limits are listed. Information for each column of the table is given below:
Column (1) observation field names that include observation date; column (2) source ID; the formats referred to the equatorial coordinates; columns (3)–(4) equatorial coordinates (J2000.0) in decimal degrees; columns (5)–(10) J, H, and K_s magnitude and error; columns (11)–(16) J, H, and $K_s$polarization degree and error in units of percentage; columns (17)–(22) J, H, and K_s polarization position angle and error in units of degrees; columns (23)–(24) absolute proper motion in right ascension and error in units of mas yr^{-1} from SPM catalog; columns (25)–(26) absolute proper motion in declination and error in units of mas yr^{-1} from SPM catalog; columns (27)–(28) Johnson B and V magnitude from SPM catalog.

[a] Only a portion of catalog is listed in Table 3. Complete source catalog is available at http://irlab.khu.ac.kr/~jaeyeong/Tab3.dat.

(This table is available in machine-readable form.)

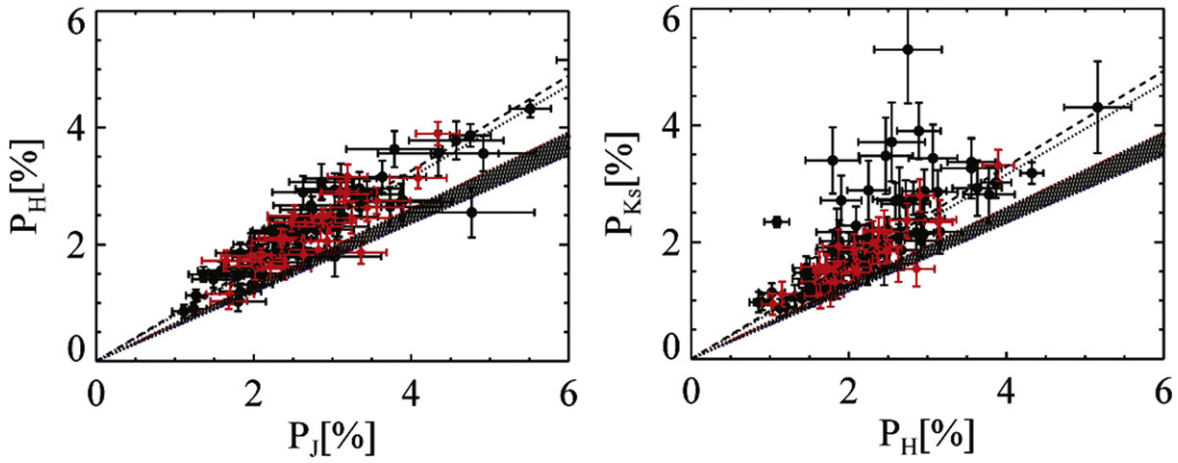

Figure 7. P_J vs. P_H (left) and P_H vs. P_{K_s} (right) for the selected 106 sources with $P/\sigma_P > 5$ and $\sigma_P \leqslant 1$ in all of the bands. The best-fit values for the slopes are $P_H/P_J = 0.81$ and $P_{K_s}/P_H = 0.82$ (dashed lines). The hatched area shows previous studies (Martin & Whittet 1990; Nagata 1990; Martin et al. 1992), and black dotted line is the best-fit value from Nakajima et al. (2007). The red symbol shows the sources matched with the *AKARI* LMC catalog.

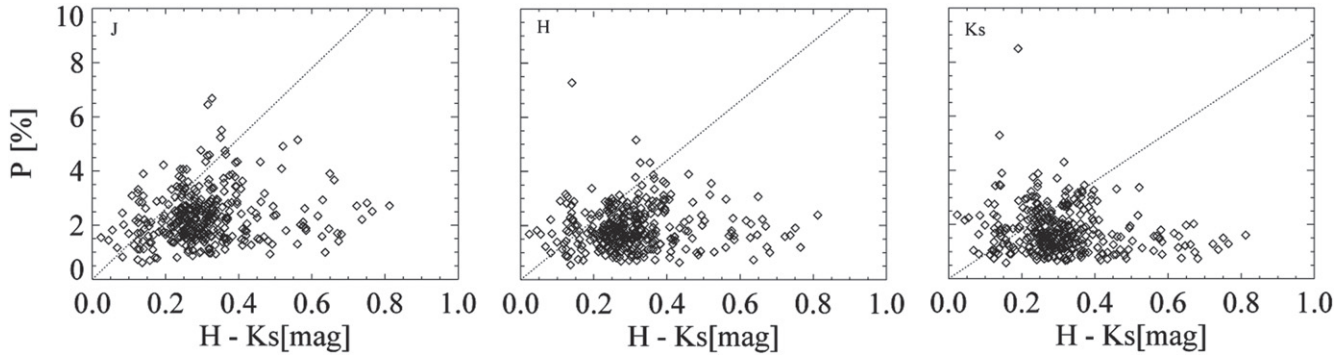

Figure 8. Degree of polarization P for the J(left), H(middle), and K_s(right) bands vs. $H - K_s$ color. Dotted lines are empirical upper limits, $P_{\max}$ (Jones 1989). Open diamonds are sources with $P/\sigma_P > 3$ and $\sigma_P \leqslant 1$ in all bands.

We examined the correlation between the observed polarization efficiency and the upper limit of polarization degree. Figure 8 shows the result of polarization efficiency for the sources with $P/\sigma_P > 3$ and $\sigma_P \leqslant 1$ in all bands. Most of the sources are located below the upper limit of interstellar polarization (dashed line). This means that the observed polarization in the LMC is of interstellar origin.

3.4. Possibility of Intrinsic Polarization Component

AGB stars are often associated with nebulosity, and therefore the polarization might be intrinsic rather than interstellar. We examine this possibility using the mid-infrared observation data of the *AKARI* LMC point-source catalog. Using a color–color diagram and a color–magnitude diagram of the five photometric bands at 3.2, 7, 11, 15, and 24 μm, Kato et al. (2012) classified the sources with dusty C-rich and O-rich AGB stars.

In our catalog, 208 sources have been matched to the *AKARI* LMC point sources in the 3.2, 7, and 11 μm bands. The matched *AKARI* sources were divided into AGB stars without dusty envelopes and dusty C-rich/O-rich AGB stars. However, distributions of the polarization degrees and position angles do not show any significant differences between the two groups. In addition, the matched *AKARI* sources do not show any different power-law relationship (Figure 7). This implies that the detected polarization is of an interstellar origin rather than being intrinsic to AGB stars.

4. DISCUSSION

4.1. Polarization Results

Figures 9 and 10 show the H-band polarization maps in the observed LMC fields. Each vector represents a point source with $P/\sigma_P > 3$. The number of selected stars was 875, 1468, and 732, in the J, H, and K_s bands, respectively. Most of these vectors are directed either from north to south or from northeast to southwest.

In the region around 30 Doradus (Figure 9), most of the polarization vectors have directions from northeast to southwest. In the southeastern region of 30 Doradus, the distribution of the polarization vectors shows a shell-like structure encircling the $n39$ field. W07 presented the magnetic field structure of NGC 2100, for which the western part overlapped our fields. The polarization feature in the region of overlap shows similar polarization vector patterns. W07 reported that the origin of the magnetic field geometry around NGC 2100 includes massive outflows moving eastward from the 30 Doradus region. The coherent pattern of the polarization vectors in the north and south of the $n39$ field is consistent with that of W07. They reported that the pattern is influenced by magnetic field lines along the eastward outflows. In addition, other patterns in the $n39$ field can be explained by the interaction between the environment of NGC 2100 and the eastward outflows. The large-scale outflow from 30 Doradus is one plausible source of the influence on the structural formation

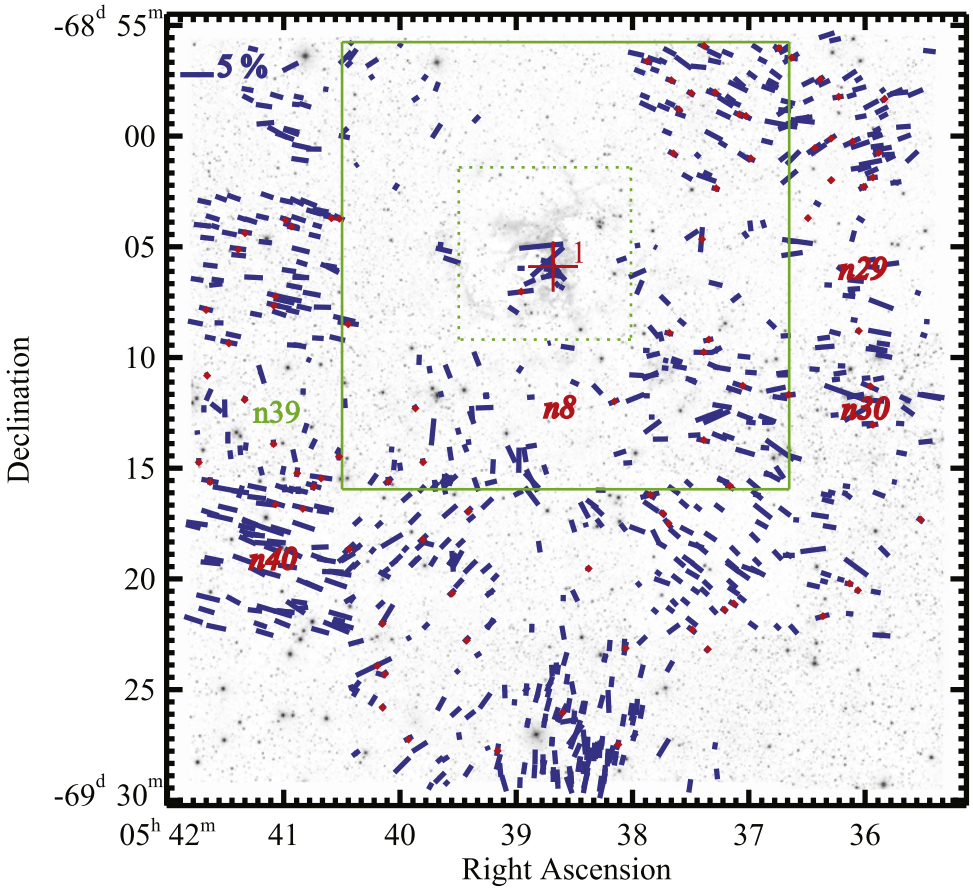

Figure 9. Polarization vector map of the *H* band for the region around 30 Doradus. Stars that have $P/\sigma_P > 3$ are displayed with blue lines. The lengths of the vectors denote the degree of polarization, and the scale is shown in upper left corner. One field overlapped with W07 and three other sample fields are denoted by the field names in red and bold. Those fields were used to calculate the magnetic field strength. The fields of view covered by N07 and Kim et al. (2011) are also highlighted as green dotted and solid boxes, respectively. The location of the optical polarimetry by W07 is the eastern side of the *n*39 field (green-colored field name). Red diamonds are the *AKARI* sources that we matched in Section 3.4. The center position of 30 Doradus is denoted by the red-colored cross with a number of 1.

of the supergiant shell on the western side of 30 Doradus (LMC 3 region). Overall vectors in the western regions of 30 Doradus show coherent patterns in the direction of the LMC 3 region identified in previous studies (Meaburn 1980; Points et al. 2001; Book et al. 2008; Dawson et al. 2013). As suggested by W07, the extended uniform patterns of the magnetic field can be an indication of large-scale outflows toward the boundaries of a supergiant shell.

The polarization vectors in Figure 10 show a complex distribution. At the eastern part, most of the polarization vectors are directed north–south. However, the vectors at the other side show a different distribution structure, more like a tilted S-shape. We suspect that these patterns of polarization vectors are related to the magnetic field lines south of 30 Doradus. Previous studies (Wayte 1990; Haynes et al. 1991; Schmidt-Kaler 1992) of the geometry of the magnetic field south of 30 Doradus suggested that it is aligned with filamentary features B and C of Figure 2 in Feitzinger et al. (1987). Two patterns show directions similar to those of these filamentary features. Wayte (1990) and Mao et al. (2012) also proposed that the gaseous H I spiral features are likely associated with the large-scale magnetic fields toward the south direction.

A statistical analysis was conducted field-by-field to understand the interstellar polarization properties. In Table 3, the number of stars with $P/\sigma_P > 3$ for each band is given in columns (2−4). The average polarization degrees for each band are given in columns (5), (7), and (9), and their mean uncertainties in columns (6), (8), and (10). The average polarization position angles at each band are given in columns (11), (13), and (15) with their standard deviations in columns (12), (14), and (16). We examined the magnetic field strength of the fields overlapped with those described by W07 and other sample fields using the analysis of Chandrasekhar & Fermi (1953), which is described by

$$B = Q\sqrt{4\pi\rho}\,\frac{\delta v_{\rm los}}{\delta\theta}, \tag{7}$$

where ρ is the mean density, $\delta v_{\rm los}$ is the velocity dispersion in the line of sight, and $\delta\theta$ is the dispersion in the Gaussian fit of the polarization position angles. Kim et al. (2007) presented a 21 cm neutral hydrogen interferometric survey of the LMC in a catalog of H I gas clumps or clouds with 16, 32, and 64 K brightness temperature thresholds. By matching their catalog locations with the positions of our observed fields, we obtained $\delta v_{\rm los}$ from their survey results. The applied $\delta v_{\rm los}$ of the matched sample fields are tabulated in Table 4. As Crutcher (2004) reported, the value of a factor of the order of unity, Q, shows the best result when the value from Ostriker et al. (2001) is adopted. By simulation, Ostriker et al. (2001) determined that Q is approximately 0.46−0.51, when the observed dispersions

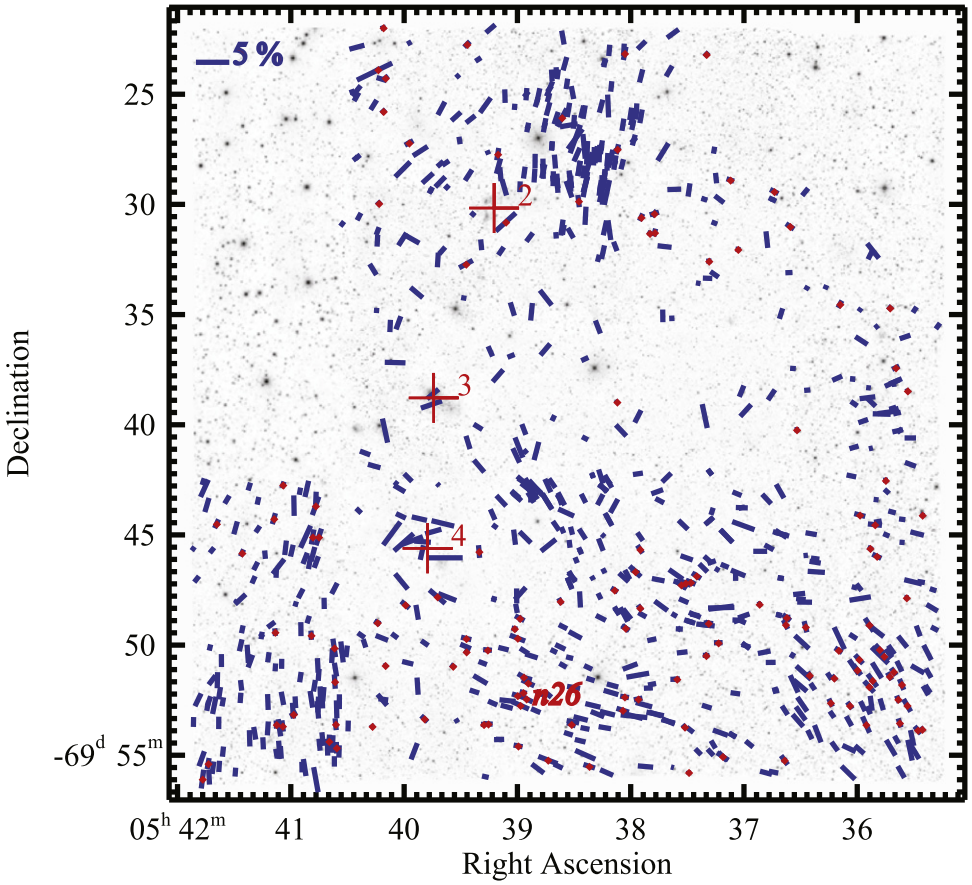

Figure 10. Same as in Figure 9, but for regions around N158, N160, N159, and the southern field. The center positions of N158, N160, and N159 are denoted by the red crosses with numbers from 2 to 4, respectively. One sample field to calculate the magnetic field strength is denoted by the field name in red and bold.

in polarization position angles indicate relatively strong magnetic field strengths ($\delta\theta < 25°$). We set the value of Q to be 0.5, as suggested by Crutcher (2004). We used column (14) in Table 3 to select sample fields showing a coherent distribution of polarization position angles. For the coherent distribution, $\delta\theta$was calculated by a Gaussian fit centered at the average polarization position angles in Table 3. We tested whether the distribution of the polarization position angles is well fit to a Gaussian distribution by applying the Martinez–Iglewicz normality test (Martinez & Iglewicz 1981),

$$I = \frac{\sum_{i=1}^{n}\left(\theta_i - \langle\theta_H\rangle\right)^2}{(n-1)\delta\theta^2} \quad (8)$$

where I is the Martinez–Iglewicz test statistic and $\langle\theta_H\rangle$ is average polarization position angles in the H band. If the distribution significantly deviates from normal, then it indicates the presence of possible sub-structure. To eliminate these cases, we selected fields showing test values I close to $'1'$ (Table 4). W07 used the H I number density from Points et al. (1999) to estimate the mean density in their observed fields. We also assumed a number density of 4 cm^{-3} as used in W07. As seen in Table 4, we tabulated the magnetic field strengths for the five sample fields. One of them is the same region considered in W07, and it shows a similar magnetic field strength. The derived magnetic field strengths and sizes of the selected regions are similar to the properties of a typical cloud complex (i.e., scale 10−100 parsecs and magnetic field strength ranging from 10 to 30 μG) as reported by Chapman et al. (2011).

4.2. Polarization Structure with Molecular Cloud Studies

In order to understand the pattern of polarization vectors, we examined our H-band polarization map by comparing the literature on mid- to far-infrared dust emission maps and CO gas emission maps. We assume that the position angle of polarization indicates the direction of the magnetic field because the observed polarization originated from interstellar dust grains with the short axis aligned with the local magnetic field in the LMC.

The IRAC data (3.6, 5.8, and 8 μm) from the *Spitzer* SAGE (Meixner et al. 2006) were compiled to trace dust emission features in the LMC fields more clearly. Although we have performed a comparison with the Herschel data (100, 160, and 250 μm) from the HERITAGE project (Meixner et al. 2010), we did not find any features different from those in the *Spitzer* data due to relatively poor resolution. The IRAC data are displayed as a color composite image (shown in Figures 11 and 12), and we overlaid our polarization vector map on these figures. The polarization vectors showing prominent patterns indicate the direction of the local magnetic field lines and we indicated these patterns with a green shaded curve in both Figures 11 and 12.

The overall trend of the polarization vectors shows an east–west direction across the 30 Doradus region (P1 in Figure 11). Other distinctive patterns of polarization vectors are located at

Table 3
Statistical Distribution of Polarization Properties at Each Field

Field name	Number			$\langle P_J \rangle$	$\langle \sigma_J \rangle$	$\langle P_H \rangle$	$\langle \sigma_H \rangle$	$\langle P_{K_s} \rangle$	$\langle \sigma_{K_s} \rangle$	$\langle \theta_J \rangle$	$\langle \sigma_J \rangle$	$\langle \theta_H \rangle$	$\langle \sigma_H \rangle$	$\langle \theta_{K_s} \rangle$	$\langle \sigma_{K_s} \rangle$
	J	H	K_s	(%)	(%)	(%)	(%)	(%)	(%)	(°)	(°)	(°)	(°)	(°)	(°)
(1)	(2)	(3)	(4)	(5)	(6)	(7)	(8)	(9)	(10)	(11)	(12)	(13)	(14)	(15)	(16)
n1	6	15	8	1.17	0.14	0.99	0.06	1.53	0.13	140.77	50.13	139.18	10.46	138.77	11.88
n3	31	55	26	1.91	0.08	1.70	0.04	1.33	0.06	57.73	7.74	63.78	8.74	62.52	11.03
n4	14	18	10	1.47	0.11	1.30	0.08	1.86	0.18	84.18	45.32	92.96	52.09	86.87	53.53
n5	16	18	10	2.51	0.08	1.74	0.06	2.45	0.11	149.69	58.36	107.42	42.60	128.77	48.95
n6	4	3	2	1.80	0.25	1.34	0.14	1.30	0.21	78.15	7.77	75.60	6.37	83.57	18.72
n7	18	29	15	1.58	0.09	1.24	0.05	1.25	0.08	15.65	17.26	7.09	12.66	5.79	31.04
n8	15	22	15	1.98	0.10	1.53	0.06	1.08	0.07	69.46	53.88	97.91	40.94	103.47	33.55
n9	30	52	31	2.27	0.08	1.92	0.04	2.01	0.08	91.97	18.48	93.67	16.64	95.51	19.09
n10	17	60	29	1.86	0.09	1.67	0.04	1.87	0.09	47.35	6.67	51.58	8.09	49.39	15.60
n11	10	15	8	1.19	0.10	1.05	0.07	1.96	0.21	28.48	14.34	26.84	18.37	3.76	44.49
n12	28	56	25	1.78	0.07	1.57	0.04	1.37	0.08	134.81	13.19	130.56	22.64	116.69	36.68
n13	10	32	17	1.98	0.12	1.20	0.05	1.54	0.10	127.88	22.76	120.76	26.63	129.26	22.04
n14	79	99	46	2.51	0.05	1.82	0.03	1.70	0.05	10.98	13.37	9.03	17.13	11.45	21.94
n15	5	8	17	0.81	0.13	1.56	0.15	1.90	0.16	10.87	29.24	29.18	21.07	3.86	41.04
n16	6	27	13	1.05	0.11	0.89	0.04	1.15	0.11	60.02	57.63	78.98	46.74	75.73	47.31
n17	24	26	10	2.50	0.11	1.75	0.06	1.67	0.12	0.90	23.38	6.00	19.80	14.26	34.78
n18	13	20	10	1.59	0.12	1.26	0.07	1.73	0.16	1.01	32.24	15.32	33.57	6.84	19.94
n19	11	11	7	2.17	0.13	1.85	0.08	1.34	0.12	69.68	58.42	65.08	38.02	88.81	52.04
n20	8	15	8	1.99	0.17	1.12	0.08	1.35	0.15	97.36	66.20	112.08	50.86	115.97	52.49
n21	3	6	6	3.08	0.44	1.84	0.15	3.17	0.30	59.16	53.53	112.92	64.84	78.65	47.78
n22	28	60	36	2.00	0.09	1.34	0.04	1.43	0.06	65.76	23.22	71.22	29.12	73.70	40.13
n23	49	80	30	1.51	0.05	1.28	0.03	1.25	0.06	42.70	34.21	41.98	36.16	54.99	50.11
n24	14	22	14	3.07	0.14	1.56	0.06	1.39	0.08	80.27	43.90	64.97	40.29	58.17	36.28
n25	14	25	14	2.10	0.12	1.11	0.05	1.75	0.06	109.20	38.52	69.88	33.28	68.03	40.19
n26	28	53	35	2.10	0.09	1.59	0.04	1.45	0.05	65.35	11.71	71.07	8.46	69.85	16.67
n27	21	49	27	1.79	0.09	1.24	0.04	1.05	0.06	65.37	21.36	74.80	24.57	72.86	40.19
n28	28	57	25	2.17	0.10	1.87	0.04	1.67	0.07	115.04	17.10	104.52	13.30	114.09	15.46
n29	8	22	10	1.49	0.14	1.15	0.06	1.03	0.10	82.35	17.27	82.22	25.71	83.08	40.00
n30	23	33	18	2.24	0.09	2.13	0.05	1.87	0.10	76.58	19.05	82.81	13.06	90.63	30.38
n31	7	25	2	1.21	0.15	1.27	0.06	3.23	0.71	64.53	18.35	73.36	13.93	65.86	4.60
n33	2	12	8	1.10	0.28	0.98	0.07	2.25	0.20	155.01	9.73	107.10	32.60	95.92	35.90
n34	22	29	15	1.42	0.08	0.96	0.04	1.19	0.09	91.48	35.04	97.69	24.22	93.37	37.09
n35	16	36	10	1.34	0.09	1.06	0.04	0.92	0.08	69.54	16.82	79.05	13.93	75.85	14.42
n36	52	69	29	2.10	0.07	1.58	0.04	1.36	0.06	34.89	14.35	33.31	11.71	43.49	45.81
n37	6	19	5	2.73	0.26	1.77	0.09	2.61	0.34	69.02	9.05	77.33	12.33	83.17	16.88
n38	47	67	34	2.47	0.06	2.22	0.03	1.88	0.06	77.69	5.84	77.79	6.04	75.34	13.16
n39	17	31	12	1.32	0.08	1.11	0.04	1.01	0.08	0.59	38.90	0.71	26.83	6.30	24.68
n40	59	68	34	3.21	0.08	2.81	0.05	2.88	0.09	71.11	9.61	75.28	7.41	73.34	12.89
n44	31	43	22	1.64	0.08	1.52	0.04	1.40	0.07	159.21	29.87	155.54	41.15	155.62	25.22
n45	55	81	39	2.13	0.06	1.74	0.03	1.41	0.06	1.98	9.26	1.20	10.88	1.40	20.00

Notes. Information for each column of the table is given below:
Column (1) Observation field names; columns (2)–(4) the number of stars with $P/\sigma_P > 3$ for each band; columns (5), (7), (9) the average polarization degrees for each band; columns (6), (8), (10) the mean uncertainties of polarization degrees for each band; columns (11), (13), (15) the average polarization position angles for each band; columns (12), (14), (16) the standard deviation of polarization position angles for each band.

Table 4
Magnetic Field Properties at Sample Fields

Field Name	Number of Samples	$\delta v_{\rm los}$ (km s^{-1})	$\delta\theta$ (θ)	Normality Test Value	B (μG)	B_{W07}[a] (μG)
n8	22	1.4	15	0.92	3	⋯
n26	54	8.0	9	0.95	25	⋯
n29	22	1.5	16	1.42	3	⋯
n30	33	3.3	13	1.02	7	⋯
n40	69	4.8	8	1.01	19	30[b]

Notes.
[a] Magnetic field strength from W07.
[b] Region D.

the outskirts of the field of 30 Doradus, associated with dust emission features (P2, P3, and P4 in Figure 11). P2 is located at the northwestern boundary of the dust emission feature and shows a U-shaped structure. N07 found a similar U-shaped structure of polarization vectors, and they proposed that expanding shells in 30 Doradus affected complex cloud structures and the associated magnetic field. P3 and P4 exhibit apparent patterns with similar directions to those of bright emission features.

Figure 12 shows the distribution of polarization vectors mainly following the molecular cloud ridge around the star-forming regions N158, N160, and N159. The vectors located at pattern P1 show distinct elongation extending southward, with a direction similar to that of the dust emission structure. P2 also shows a uniform pattern directed in the north–south direction,

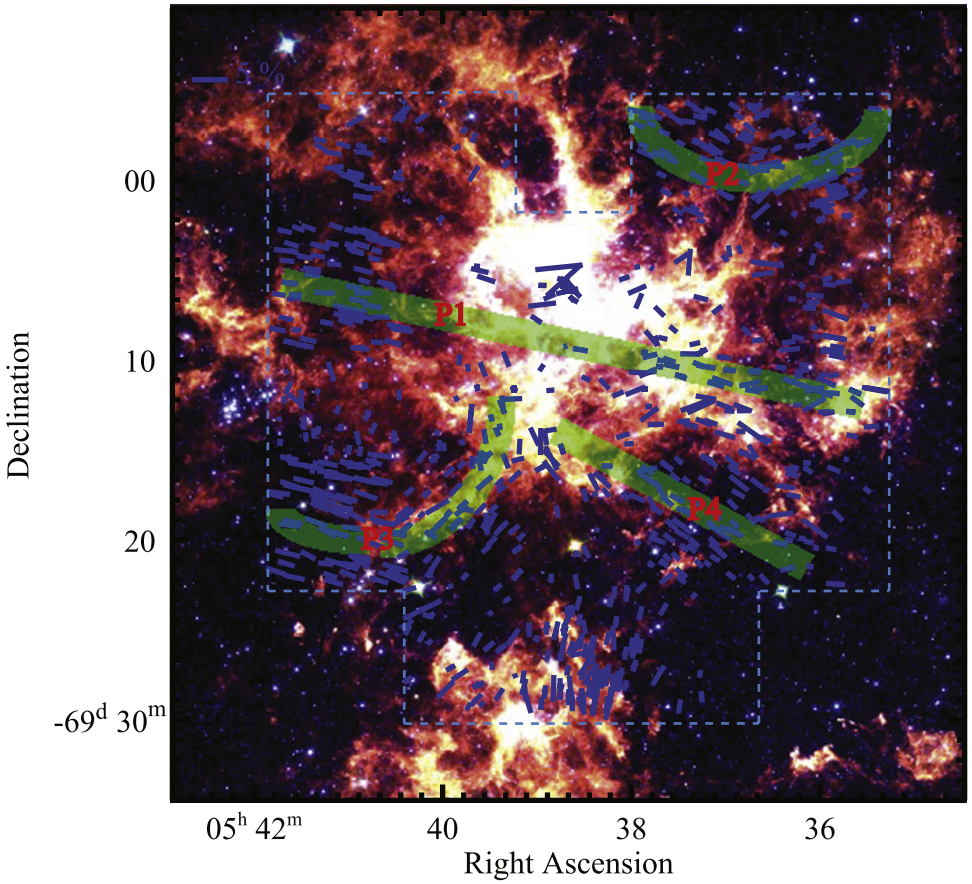

Figure 11. Distribution of polarization vectors ($P > 3\sigma_P$) from H-band data overlaid on the color composite image of *Spitzer* IRAC 3.6 (*blue*), 5.8 (*green*), and 8 μm (*red*) bands in the 30 Doradus region. Stars which $P/\sigma_P > 3$ are displayed in blue lines. Prominent patterns of polarization vectors are described as the green shaded curves (P1, P2, P3, and P4). The length of the lines denotes the degree of polarization for which the scale is shown in the upper left corner. The blue dashed box denotes the border of our data fields.

but its shape is slightly curved along the dust emission feature. These patterns (P1 and P2) are regarded as magnetic field lines related to the extended feature of the molecular cloud ridge. However, polarization vectors located at the southwestern part of Figure 12 show patterns different from those of the eastern part. Polarization vectors in patterns P3 and P4 tend to be aligned in a tilted S-shape and east–west, respectively. We observed that the dust emission feature in the southwestern part of Figure 12 seems to be extended in this direction.

On the other hand, polarization vectors in the star-forming regions (central part of 30 Doradus in Figure 11 and bright emission features in Figure 12) do not show any significant pattern. This is thought to be due to the turbulent and complex magnetic fields of the sub-structures in the star-forming region. To verify the structure of the expected turbulent magnetic fields, more detailed polarimetric data are required.

We also performed a comparison with a velocity-integrated contour map of ^{12}CO emission. NANTEN ^{12}CO(J = 1–0) emissions have been detected in giant molecular cloud complexes in the LMC (Fukui et al. 2008). Although prominent ^{12}CO emission features are located in the central 30 Doradus region, and in star-forming regions in the southern molecular cloud ridge, close correlation between the magnetic fields and ^{12}CO emission features was not found.

We conclude that the observed polarization vectors reflect a dust cloud structure resulting in polarization by dichroic extinction, and that they trace magnetic fields associated with dust clouds around star-forming region.

5. SUMMARY AND CONCLUSIONS

We conducted near-IR imaging polarimetry for a large areal region covering ($\sim$39′ × 69′) on the eastern side of the LMC. We made a band-merged catalog of photometric and polarimetric data in the J, H, and K_s bands. In this catalog, we compiled 1858 stars in the region, brighter than 14 mag in the H band and $P/\sigma_P > 3$ for least one band. The magnitude, polarization degree, and polarization position angle were listed in the catalog. In addition, we provided information on the absolute proper motion and magnitudes of B and V matched from SPM data. Using this catalog, we obtained polarization vector maps and conducted a statistical analysis of the polarization for the fields observed in the LMC. Previous similar catalogs did not cover such a large continuous area of the LMC (e.g., $\sim$15′ × 15′ by W07) or use the infrared range. Therefore, this catalog is a unique, up-to-date collection of polarization measurements for the LMC region.

The degree of polarization for the 106 sources in our catalog shows wavelength dependences similar to those reported by N07. We conclude that most of the sources in our catalog exhibit interstellar polarization, and that the dominant polarization mechanism is the result of dichroic extinction by dust grains aligned along magnetic fields, rather than due to intrinsic

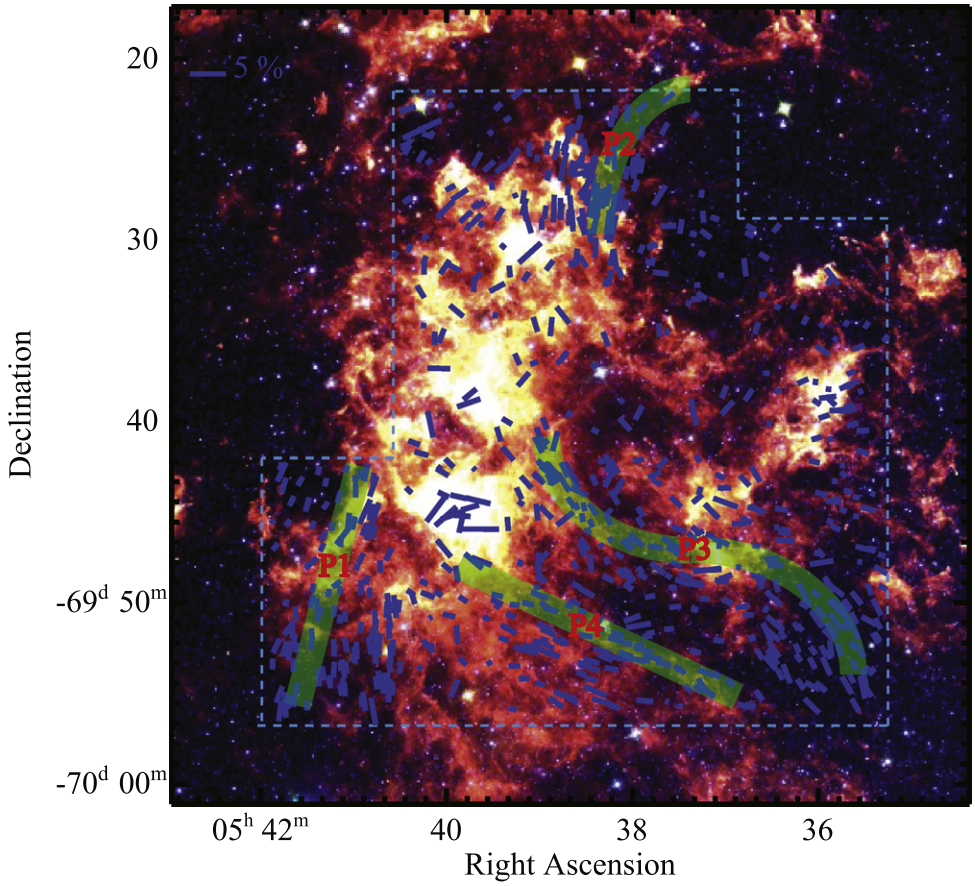

Figure 12. Same as in Figure 11, but for regions N158, N160, N159, and the southern field.

polarization of stars. Using the polarization vector maps, we traced the correlation of the polarization and the large-scale magnetic field structures in the observed regions. The geometry of the large-scale magnetic field structures around 30 Doradus, and of the southern star-forming regions, show relationships with the environment of nearby supergiant shells and the gaseous spiral features toward the south, respectively. The estimated magnetic field strengths for the selected fields (within 100 parsecs) are in the range 3−25 μG, as determined by the Chandrasekhar–Fermi method. Judging from their size and magnetic field strength, those regions are regarded as a cloud complex associated with a nebula in the LMC. Prominent patterns of polarization vectors mainly follow dust emission features in the mid- to far-infrared bands, which implies that the large-scale magnetic fields are highly involved in the structures of the dust cloud in the LMC, except for the dense star-forming regions. The cross matching of the data in this catalog with data in other catalogs for the LMC will provide useful information for probing the structure of magnetic fields and other astrophysical phenomena.

This work was supported by the National Research Foundation of Korea (NRF) grant, No. 2008-0060544, funded by the Korea government (MSIP). This work was supported in part by the Korea Astronomy and Space Science Institute (KASI). We thank an anonymous referee for valuable comments and suggestions, which significantly contributed to improving the paper. We thank Jungmi Kwon for giving us a chance to study this work. We thank Prof. Shuji Sato for kindly providing comments to improve this paper. This paper uses observations performed at the SAAO. This publication makes use of data products from the Two Micron All Sky Survey and observations with *AKARI*. The Two Micron All Sky Survey is a joint project of the University of Massachusetts and the Infrared Processing and Analysis Center/California Institute of Technology, funded by the National Aeronautics and Space Administration and the National Science Foundation. The *AKARI* is a JAXA project with the participation of ESA. This research has made use of the NASA/IPAC Infrared Science Archive, which is operated by the Jet Propulsion Laboratory, California Institute of Technology, under contract with the National Aeronautics and Space Administration.

REFERENCES

Bertin, E., & Arnouts, S. 1996, A&AS, 117, 393
Book, L. G., Chu, Y.-H., & Gruendl, R. A. 2008, ApJS, 175, 165
Chandrasekhar, S., & Fermi, E. 1953, ApJ, 118, 113
Chapman, N. L., Goldsmith, P. F., Pineda, J. L., et al. 2011, ApJ, 741, 21
Crutcher, R. M. 2004, in The Magnetized Interstellar Medium, ed. B. Uyaniker, W. Reich & R. Wielebinski (Katlenburg-Lindau: Copernicus), 123
Davis, L., Jr., & Greenstein, J. L. 1951, ApJ, 114, 206
Dawson, J. R., McClure-Griffiths, N. M., Wong, T., et al. 2013, ApJ, 763, 56
Feitzinger, J. V., Haynes, R. F., Klein, U., et al. 1987, Vistas Astron, 30, 243
Fukui, Y., Kawamura, A., Minamidani, T., et al. 2008, ApJS, 178, 56
Gaensler, B. M., Haverkorn, M., Staveley-Smith, L., et al. 2005, Sci, 307, 1610
Haynes, R. F., Klein, U., Wayte, S. R., et al. 1991, A&A, 252, 475
Jones, T. J. 1989, ApJ, 346, 728
Kandori, R., Kusakabe, N., Tamura, M., et al. 2006, Proc. SPIE, 6269, 159
Kato, D., Ita, Y., Onaka, T., et al. 2012, AJ, 144, 179
Kato, D., Nagashima, C., Nagayama, T., et al. 2007, PASJ, 59, 615
Kim, J., Pak, S., Choi, M., et al. 2011, JKAS, 44, 135

Kim, S., Rosolowsky, E., Lee, Y., et al. 2007, ApJS, 171, 419
Kim, S., Staveley-Smith, L., Dopita, M. A., et al. 1998, ApJ, 503, 674
Lazarian, A. 2007, JQSRT, 106, 225
Mao, S. A., McClure-Griffiths, N. M., Gaensler, B. M., et al. 2012, ApJ, 759, 25
Martin, P. G., Adamson, A. J., Whittet, D. C. B., et al. 1992, ApJ, 392, 691
Martin, P. G., & Whittet, D. C. B. 1990, ApJ, 357, 113
Martinez, J., & Iglewicz, B. 1981, Biometrika, 68, 331
Mathewson, D. S., & Ford, V. L. 1970, ApJ, 160, 43
Meaburn, J. 1980, MNRAS, 192, 365
Meixner, M., Galliano, F., Hony, S., et al. 2010, A&A, 518, L71
Meixner, M., Gordon, K. D., Indebetouw, R., et al. 2006, AJ, 132, 2268
Nagata, T. 1990, ApJ, 348, 13
Nagayama, T., Nagashima, C., Nakajima, Y., et al. 2003, Proc. SPIE, 4841, 459
Nakajima, Y., Kandori, R., Tamura, M., et al. 2007, PASJ, 59, 519 (N07)
Ostriker, E. C., Stone, J. M., & Gammie, C. F. 2001, ApJ, 546, 980
Pak, S., Jaffe, D. T., van Dishoeck, E. F., et al. 1998, ApJ, 498, 735
Points, S. D., Chu, Y.-H., Kim, S., et al. 1999, ApJ, 518, 298
Points, S. D., Chu, Y.-H., Snowden, S. L., & Smith, R. C. 2001, ApJS, 136, 99
Sato, S., Tamura, M., Nagata, T., et al. 1988, MNRAS, 230, 321
Schmidt, T. 1970, A&A, 6, 294
Schmidt, T. 1976, A&AS, 24, 357
Schmidt-Kaler, T. 1992, in ASP Conf. Ser. 30, Varible Stars and Galaxies, ed. B. Warner (San Francisco, CA: ASP), 207
Serkowski, K., Mathewson, D. S., & Ford, V. L. 1975, ApJ, 196, 261
Skrutskie, M. F., Cutri, R. M., Stiening, M. D., et al. 2006, AJ, 131, 1163
Tamura, M., Nagata, T., Sato, S., & Tanaka, M. 1987, MNRAS, 224, 413
Tamura, M., Nagata, T., Sato, S., et al. 1988, MNRAS, 231, 445
Vieira, K., Girard, T. M., van Altena, W. F., et al. 2010, AJ, 140, 1934
Visvanathan, N. 1966, MNRAS, 132, 423
Vrba, F. J., Strom, S. E., & Strom, K. M. 1976, AJ, 81, 958
Wayte, S. R. 1990, ApJ, 355, 473
Whittet, D. C. B., & van Breda, I. G. 1978, A&A, 66, 57
Wisniewski, J. P., Bjorkman, K. S., Magalhães, A. M., & Pereyra, A. 2007, ApJ, 664, 296 (W07)